nature energy

ARTICLES

https://doi.org/10.1038/s41560-019-0355-9

Chemical and structural origin of lattice oxygen oxidation in Co–Zn oxyhydroxide oxygen evolution electrocatalysts

Zhen-Feng Huang[1], Jiajia Song[2,3], Yonghua Du[4], Shibo Xi[4], Shuo Dou[1], Jean Marie Vianney Nsanzimana[1], Cheng Wang[5], Zhichuan J. Xu[2]* and Xin Wang[1]*

The oxygen evolution reaction (OER) is a key process in electrochemical energy conversion devices. Understanding the origins of the lattice oxygen oxidation mechanism is crucial because OER catalysts operating via this mechanism could bypass certain limitations associated with those operating by the conventional adsorbate evolution mechanism. Transition metal oxyhydroxides are often considered to be the real catalytic species in a variety of OER catalysts and their low-dimensional layered structures readily allow direct formation of the O–O bond. Here, we incorporate catalytically inactive Zn^{2+} into CoOOH and suggest that the OER mechanism is dependent on the amount of Zn^{2+} in the catalyst. The inclusion of the Zn^{2+} ions gives rise to oxygen non-bonding states with different local configurations that depend on the quantity of Zn^{2+}. We propose that the OER proceeds via the lattice oxygen oxidation mechanism pathway on the metal oxyhydroxides only if two neighbouring oxidized oxygens can hybridize their oxygen holes without sacrificing metal–oxygen hybridization significantly, finding that $Zn_{0.2}Co_{0.8}OOH$ has the optimum activity.

Mechanistic understanding of the oxygen evolution reaction (OER) is crucial for the development of efficient OER electrocatalysts, because of its key role in the anodic reaction of various electrochemical systems for sustainable conversion of renewable energy into chemical fuels[1–3]. In the conventional adsorbate evolution mechanism (AEM), the OER involves multiple adsorbed intermediates that exhibit highly correlated adsorption strength, leading to a minimum theoretical overpotential of about 0.37 V[2,4–7]. A recently identified mechanism for perovskite oxides[8–13], the lattice oxygen oxidation mechanism (LOM), which involves direct O–O coupling, has been suggested to be able to bypass this limitation[14,15], and a catalyst based on LOM can potentially offer much better OER activity. Strikingly, the anionic redox process is a common phenomenon and has been thoroughly investigated in gas-phase catalytic reactions and lithium-rich oxide cathodes[15–17]. However, the chemical and structural origin leading to the LOM is not fully understood, preventing the rational design of such OER electrocatalysts.

Transition metal oxyhydroxides (MOOH, where M = Fe, Co or Ni) are often the real catalytically active species generated from irreversible surface reconstruction on many types of oxygen-evolving materials[18–25]. Moreover, the low-dimensional layered structure of MOOH provides sufficient structural flexibility for the LOM, unlike three-dimensional structured oxides that only allow surface formation of O–O bonds because of the low bulk flexibility[26]. Thus, MOOH is one of the most representative platforms for directly investigating the chemical and structural origin of the LOM.

Here, we use CoOOH as a model material, in which low-valence and catalytically inactive $Zn^{2+}(d^{10})$[27] ions are incorporated to form accessible oxygen non-bonding (O_{NB}) states with different local configurations. Combining theoretical and experimental approaches, we reveal that creating oxygen holes in O_{NB} states along the specific local configuration is critical to regulating the OER mechanism. Specifically, we suggest that the switch of the OER mechanism from the AEM to the LOM occurs only if two neighbouring oxidized oxygens can hybridize their oxygen holes without sacrificing metal–oxygen hybridization significantly. In addition, the reversible oxygen vacancy refilling process is found to be associated with the specific local configuration and determines the stability of the catalyst. More importantly, such understanding of the LOM offers a guideline for the development of efficient catalysts towards water oxidation or other heterogeneous catalysis participated by lattice oxygen.

Formation of oxygen holes in O_{NB} states

All three O(2*p*) orbitals (Supplementary Fig. 1) are engaged in M–O bond formation in MOOH, resulting in (M–O) bonding bands ($a_{1g}/t_{1u}/e_g/t_{2g}$, with oxygen character) and (M–O)* antibonding bands ($a_{1g}^*/t_{1u}^*/e_g^*/t_{2g}^*$, with metal character)[28,29]. The energy difference between (M–O) and (M–O)*, called the charge transfer energy (Δ), depends on the electronegativity difference (Δχ) between metal and oxygen ions. Moreover, for late transition metal oxides[29], the strong *d*–*d* Coulomb interaction (*U*) splits the (M–O)* antibonding band with one empty upper-Hubbard band (UHB) and one filled lower-Hubbard band (LHB). *U* is inversely proportional to the orbital volume and hence strongly depends on the valence state of the metal. In MOOH ($U < \Delta$), the electron can be first removed from the filled LHB with the increased valence state of the metal after the initial

---

[1]School of Chemical and Biomedical Engineering, Nanyang Technological University, Singapore, Singapore. [2]School of Materials Science and Engineering, Nanyang Technological University, Singapore, Singapore. [3]Singapore-HUJ Alliance for Research and Enterprise, NEW-CREATE Phase II, Campus for Research Excellence and Technological Enterprise (CREATE), Singapore, Singapore. [4]Institute of Chemical and Engineering Sciences, A*STAR, Singapore, Singapore. [5]Institute for New Energy Materials and Low-Carbon Technologies, Tianjin University of Technology, Tianjin, China. *e-mail: xuzc@ntu.edu.sg; WangXin@ntu.edu.sg

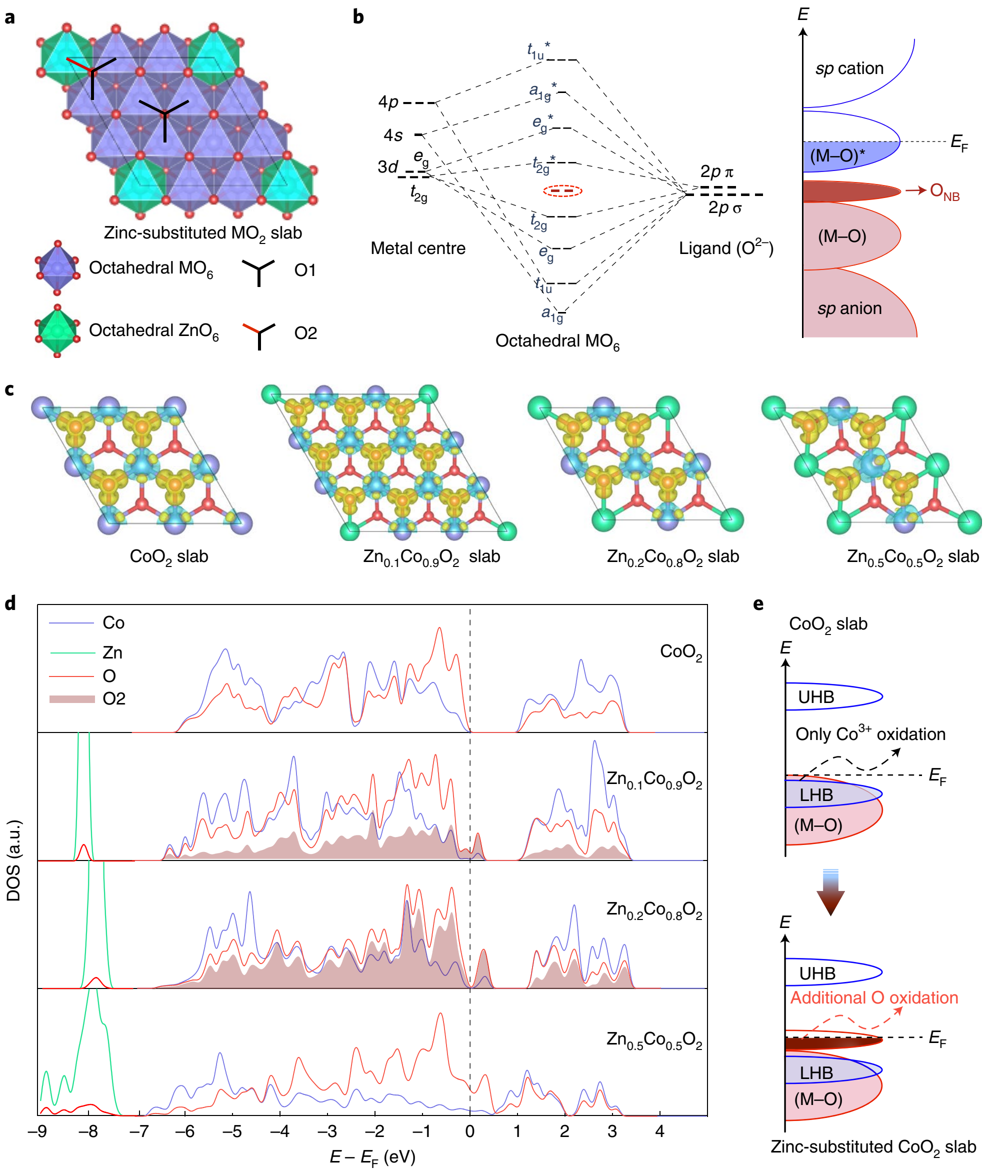

Fig. 1 | Formation of oxygen holes in O_{NB}. **a**, Model of zinc-substituted MO_2. Purple, green and red balls represent metal, zinc and oxygen atoms, respectively. **b**, Schematic formation of O_{NB} by extrapolating the molecular orbital energy diagram for octahedral MO_6. E_F represents the Fermi level. **c**,**d**, Charge density difference (**c**) and projected DOS (**d**) of CoO_2 and zinc-substituted CoO_2 slabs. Yellow and blue colours represent charge accumulation and depletion, respectively, with an iso-surface value of 0.015 eÅ^{-3}. **e**, Schematic energy bands of CoO_2 and zinc-substituted CoO_2 slabs in consideration of Mott–Hubbard splitting.

electrochemical deprotonation. The increased valence state of the metal then reduces the electronegativity difference and enhances the *d*–*d* Coulomb interaction, leading to $U > \Delta$ and making the LHB enter into the (M–O) bonding band (Supplementary Fig. 2). Further removed electrons have to mainly originate from the (M–O) bonding band, resulting in possible structural destabilization due to the decreased M–O bond order.

From the viewpoint of structural stability, two necessary conditions need to be met simultaneously to trigger lattice oxygen oxidation in oxide-based electrocatalysts[28,29]: (1) introduction of a buffer band from O_{NB} states (Fig. 1a,b), in which the M–O bond maintains its initial bond order even if the electrons are removed from O_{NB}; and (2) high covalency of the M–O bond, to ensure the removal of electrons from O_{NB} instead of LHB. Thus, CoOOH is employed as a model material, in which the low-valence and catalytically inactive $Zn^{2+}(d^{10})$[27] is incorporated to form the accessible O_{NB} states and increase Co–O covalency simultaneously. By systematically analysing charge density difference and density of states (DOS) in various zinc-substituted CoO_2 slabs (denoted as $Zn_xCo_{1-x}O_2$), we identified the chemical origin leading to lattice oxygen oxidation in MOOH.

The $CoO_2(001)$-terminated surface was chosen as a computational model (Supplementary Fig. 3) for two reasons. First, the (001) atomic layer is a stable and experimentally available CoOOH structure. Second, high-valent $Co^{IV}{=}O$ species on cobalt-based oxide surfaces have been detected as chemical intermediates[25,30]. Zinc is incorporated by partially replacing cobalt atoms (denoted as $Zn_xCo_{1-x}O_2$, where $x = 0.1$, 0.2 and 0.5) to further regulate the local configuration, including the oxygen bonding environment (Supplementary Fig. 3). For $Zn_{0.1}Co_{0.9}O_2$ and $Zn_{0.2}Co_{0.8}O_2$, there are two kinds of oxygen ion: (1) O1, coordinated with three cobalt ions; and (2) O2, coordinated with one zinc ion and two cobalt ions (Fig. 1a). For $Zn_{0.5}Co_{0.5}O_2$, there is another kind of oxygen ion (O3), coordinated with two zinc ions and one cobalt ion. Considering the completely filled 3*d* states of Zn^{2+}, one of the O(2*p*) orbitals pointing towards the zinc in $Zn_xCo_{1-x}O_2$ is weakly bonded because of its relatively small overlap with the Zn(3*d*) orbital. This is confirmed by the charge density difference and projected DOS (pDOS) of the Zn(3*d*) orbitals in the zinc-substituted CoO_2 slab (Fig. 1c,d), in which significant electron localization around the oxygen along the Zn–O bond and no obvious electronic states of Zn(3*d*) orbitals near E_F can be found. Additionally, from the pDOS of O(2*p*) orbitals, large amounts of high-energy O_{NB} states are generated, which are associated with the O2 or O3 bonding environment. Moreover, more unoccupied oxygen states from O_{NB} above E_F are present with the increase of zinc from $x=0.1$ to $x=0.5$. As a result, the appearance of Zn–O bonds pushes these weakly bound O_{NB} states in CoO_2 relatively higher in energy, as shown in Fig. 1b[28,29,31]. Moreover, the magnetization moments of oxygen ions (that is, O2 and O3) for $Zn_xCo_{1-x}O_2$ are increased to about 0.212 and 0.418 μ_B compared with CoO_2 (0.047 μ_B), indicating that the increase in zinc leads to more oxygen holes (Supplementary Table 1)[28,32]. All of these indicate that the oxygen holes with radical character are generated due to insufficient electron donation from zinc[26]. As the hole on an oxygen ion is direct evidence of oxygen oxidation, these results suggest that extraction of labile oxygen electrons from O_{NB} is the chemical origin of lattice oxygen oxidation (Fig. 1e)[26,28,29].

Conditions of the LOM

We now discuss the conditions under which the oxidized oxygen ions with oxygen holes could couple into O–O bonds directly, leading to the preferential LOM. As known, oxygen holes in O_{NB} can promote both direct O–O coupling (the LOM) and nucleophilic OH^- attack (the AEM)[32,33]. Herein, we systematically correlated OER energetics in the AEM and LOM pathways with different local configurations by controlling the zinc amount (for example, Co–O1–Co–O1–Co for CoO_2, Co–O2–Zn–O2–Co and Zn–O2–Co–O1–Co for $Zn_{0.1}Co_{0.9}O_2$, Zn–O2–Co–O2–Zn for $Zn_{0.2}Co_{0.8}O_2$ and Zn–O3–Co–O2–Zn for $Zn_{0.5}Co_{0.5}O_2$, as shown in Supplementary Figs. 4–6). Also, the energetics for the oxygen vacancy refilling in the LOM pathway with different local configurations are discussed.

The five elementary steps, including four electrochemical steps and one non-electrochemical O_2 desorption step, in the AEM and LOM pathways are shown in Fig. 2a, with O–Co–O(OH) (Supplementary Figs. 5 and 6) as a unified starting point. As seen, step 1 differentiates between the AEM and LOM. Therefore, the relative stabilities (free energy difference, ΔG) between the two isomeric intermediates of A2 and L2 and the activation free energy ($\Delta G^{\ddagger}$) from A2 to L2 are key to correlating the OER mechanism with different local configurations[8,34]. For CoO_2, the OER follows the conventional AEM pathway (Fig. 2a, left), because A2 is 1.41 eV intermediate^{-1} lower in energy than L2, and the $\Delta G^{\ddagger}$ for the formation of L2 is very high, with a barrier of 2.12 eV (Fig. 2b and Supplementary Fig. 7). The formation of *OOH (where the asterisk denotes an active site on the catalyst surface) in step 2 serves as the potential-determining step (PDS; 1.46 eV), consistent with the previous studies[32,35]. For $Zn_{0.1}Co_{0.9}O_2$, corresponding to Zn–O2–Co–O1–Co and Co–O2–Zn–O2–Co, the OER still follows the AEM pathway. On Zn–O2–Co–O1–Co, A2 is 0.22 eV intermediate^{-1} lower in energy than L2, with $\Delta G^{\ddagger}=1.00$ eV. On Co–O2–Zn–O2–Co, A2 is comparable to L2 in energy with only 0.04 eV intermediate^{-1} lower than L2, while $\Delta G^{\ddagger}=1.39$ eV, which is higher than that on Zn–O2–Co–O1–Co because more directional Co–O covalent bonds need to be broken (Supplementary Figs. 4b,c and 7). Moreover, the change of free energy for the formation of *OOH (0.15 eV) is decreased compared with CoO_2 (1.46 eV) due to the promoted nucleophilic OH^- attack on oxygen holes[32,33]. Meanwhile, due to the strong scaling relation '$G(*OOH)=G(*OH)+3.2$ eV' in the AEM pathway, the PDS is switched from the formation of *OOH (step 2) to the deprotonation of *OH (step 1) on $Zn_{0.1}Co_{0.9}O_2$[5]. As a result, $Zn_{0.1}Co_{0.9}O_2$ shows a decreased OER overpotential, but its value of 0.65 eV is still very high for the overall OER process. $Zn_{0.2}Co_{0.8}O_2$ and $Zn_{0.5}Co_{0.5}O_2$ both proceed via the preferential LOM pathway (Fig. 2b,c). On the one hand, L2 is intriguingly 0.52 and 2.42 eV intermediate^{-1} lower in energy than A2, respectively (Fig. 2b). On the other hand, $\Delta G^{\ddagger}$ is modest and generally surmountable at room temperature, with values of 0.46 and 0.40 eV, respectively, owing to the favourable thermodynamics and negligible sacrifice of Co–O hybridization (Supplementary Figs. 4b,c and 7). Specifically, for $Zn_{0.2}Co_{0.8}O_2$, the PDS is identified to be the deprotonation of *OH (step 4) and the corresponding OER overpotential is decreased to 0.27 eV. This indicates that the proposed LOM pathway on $Zn_{0.2}Co_{0.8}O_2$ could break the scaling relations between *OOH and *OH on the AEM pathway centred on a single metal site[5]. Unfortunately, for $Zn_{0.5}Co_{0.5}O_2$, O_2 gas could be formed spontaneously without undergoing the L2 intermediate in step 1 (Fig. 2b). Consequently, the PDS for OER on $Zn_{0.5}Co_{0.5}O_2$ becomes the subsequent oxygen vacancy refilling step with the energy barrier of 0.96 eV. Therefore, excessive substitution would not only lower the overall activity, but also lead to a severe degradation of catalyst due to the large number of oxygen losses[36]. These were confirmed by pDOS (Fig. 1d), in which the negligible electronic states of cobalt orbitals around E_F could not effectively stabilize the oxidized oxygen[37]. We also note that the kinetics of the O_2 release step are very feasible for the corresponding favourable mechanism on all of the models (Supplementary Fig. 8)[38].

All of these calculations, from the perspectives of both thermodynamics and kinetics, suggest that the σ overlap between the neighbouring O(2*p*) orbitals in the Zn–O2–Co–O2–Zn configuration is enhanced compared with the case of Co–O1–Co–O1–Co, as evidenced by the enlarged intersection angle between two neighbouring oxygen ions (Supplementary Fig. 4a)[28,37]. This can be explained by the less directional Zn–O bond compared with the Co–O bond[28,31]. The pDOS in Fig. 2d and Supplementary Fig. 9 further implies that the O–O coupling could effectively eliminate almost all of the unoccupied portions of the O_{NB} around E_F, substantially stabilizing the system (Fig. 2e)[37]. In contrast, the neighbouring oxygen atoms cannot be coupled into the O–O bond along other configurations (including Co–O1–Co–O1–Co, Zn–O2–Co–O1–Co and Co–O2–Zn–O2–Co) owing to the high energy for breaking the directional Co–O bond (Supplementary Fig. 4b,c). Therefore, we conclude that an O–O bond arises in the LOM only if two neighbouring oxidized oxygens can rotate to hybridize their oxygen holes without sacrificing metal–oxygen hybridization significantly.

Electrocatalyst preparation and characterization

In light of these findings, experiments were designed (Fig. 3a and Supplementary Figs. 10 and 11) to homogeneously incorporate different amounts of Zn^{2+} into CoOOH (denoted as $Zn_xCo_{1-x}OOH$, where $x=0.1$, 0.2, 0.3, 0.4 and 0.5) to modulate the local configuration. The X-ray diffraction (XRD) pattern (Supplementary Fig. 12) shows that the as-synthesized oxyhydroxides can be indexed as β-CoOOH (Joint Committee on Powder Diffraction Standards number 14-0673). This indicates the homogenous incorporation of zinc ions into the lattice of CoOOH by occupying the sites of cobalt ions in CoO_6 octahedra. Moreover, the diffraction peaks of $Zn_xCo_{1-x}OOH$ do not show evident shift compared with those of CoOOH, suggesting that the substitution almost does not influence the cell parameters due to the very similar ionic radius of Zn^{2+} and Co^{3+} ions[39]. Taking $Zn_{0.2}Co_{0.8}OOH$ as an example, the scanning electron microscopy (SEM) image shows that the rhombic dodecahedral morphology with an average size of 800 nm is preserved after the chemical oxidation (Fig. 3b). A closer observation of the shells demonstrates that the rougher surfaces are assembled by cross-linked nanosheets (Fig. 3b, inset). Scanning transmission electron

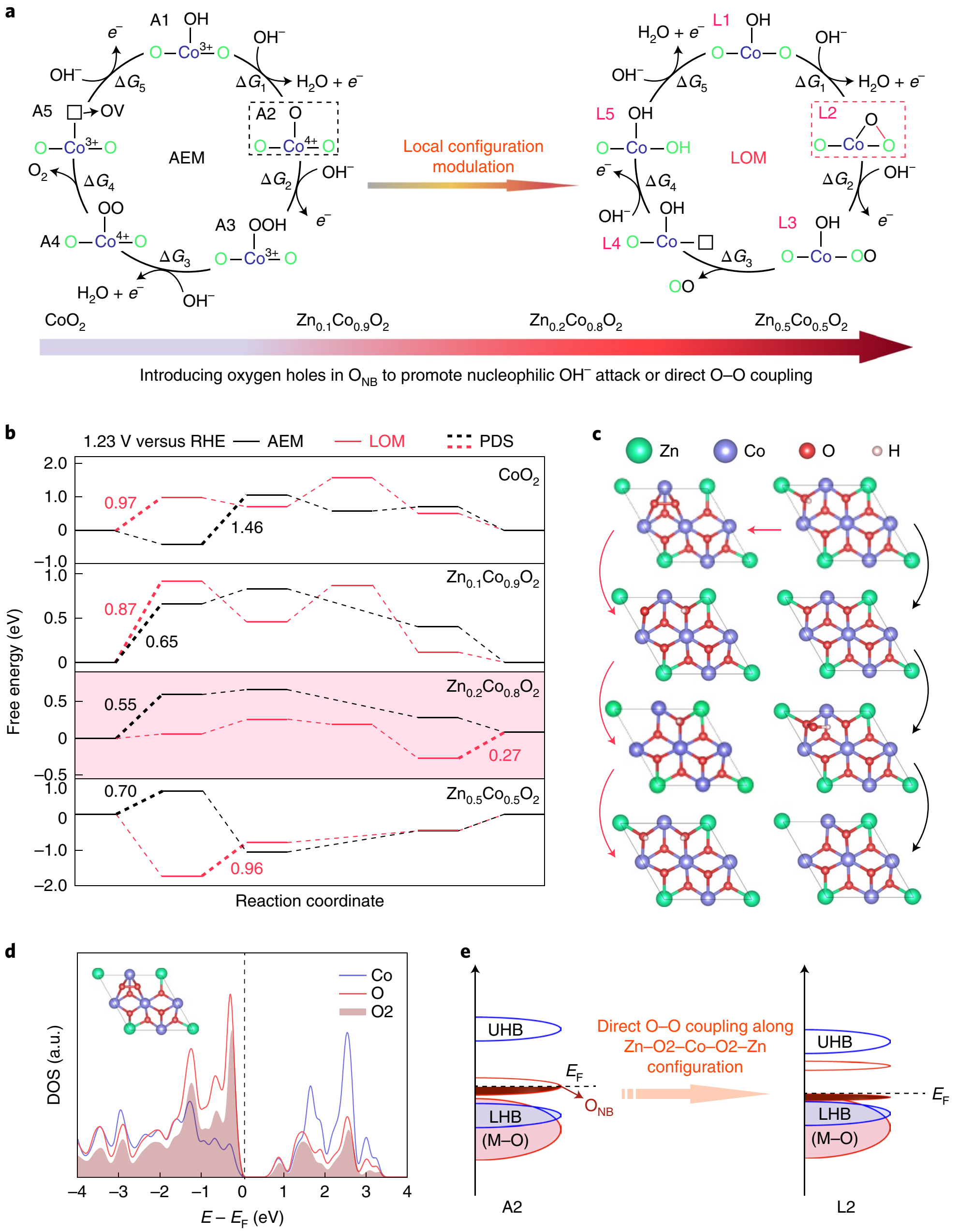

Fig. 2 | Correlation of the OER mechanism with the different local configurations. a, Proposed OER mechanisms, including AEM (left) and LOM (right). A2 and L2 are the isomeric intermediates that differentiate between the OER pathways AEM and LOM. Other related intermediates are also labelled. The empty square represents the oxygen vacancy. **b**, Free energies of OER steps via both mechanisms on CoO_2 and zinc-substituted CoO_2. **c**, Adsorption configurations for the LOM (red arrows) and AEM (black arrows) over $Zn_{0.2}Co_{0.8}O_2$. **d**, pDOS of O(2*p*) and Co(3*d*) orbitals in the L2 intermediate for $Zn_{0.2}Co_{0.8}O_2$. **e**, Switching of the OER mechanism to the LOM with the elimination of unoccupied oxygen states in $Zn_{0.2}Co_{0.8}O_2$.

microscopy (STEM) electron energy-loss spectroscopy (EELS) element mapping (Fig. 3c) further confirms the uniform distribution of zinc, cobalt and oxygen of oxyhydroxides with a Zn/Co ratio identical to corresponding ZnCo metal–organic frameworks (MOFs), in agreement with inductive coupled plasma (ICP) results (Supplementary Table 2). The similar morphologies of other zinc-substituted CoOOH structures are shown in Supplementary Fig. 13.

We further investigated the influence of zinc incorporation on the electronic and coordination structures of CoOOH from bulk to surface using X-ray absorption fine-structure spectroscopy (XAFS) and X-ray photoelectron spectroscopy (XPS). From cobalt K-edge extended XAFS (EXAFS) $k^2\chi(R)$ spectra (Fig. 3d)[40], the intensity of the Co–M peak (2.41 Å) for CoOOH shows negligible change after incorporating zinc, indicating that Zn^{2+} ions (confirmed by the Zn(2*p*) XPS spectrum in Supplementary Fig. 14) homogenously substitute for the Co^{3+} sites of CoO_6 octahedra without changing the coordination geometry. Strikingly, the intensity of the Co–O peak (1.48 Å) and fitted Co–O coordination number (Supplementary Table 3) for $Zn_{0.2}Co_{0.8}OOH$ are much lower than those of CoOOH, suggesting the presence of oxygen vacancies in bulk. Figure 3e presents the normalized cobalt K-edge XANES spectra of $Zn_xCo_{1-x}OOH$ (where $x = 0$, 0.1, 0.2 or 0.3). The broad pre-edge peak with the decreased intensity compared with CoOOH indicates preservation of the octahedra symmetry ligand field[40–42].

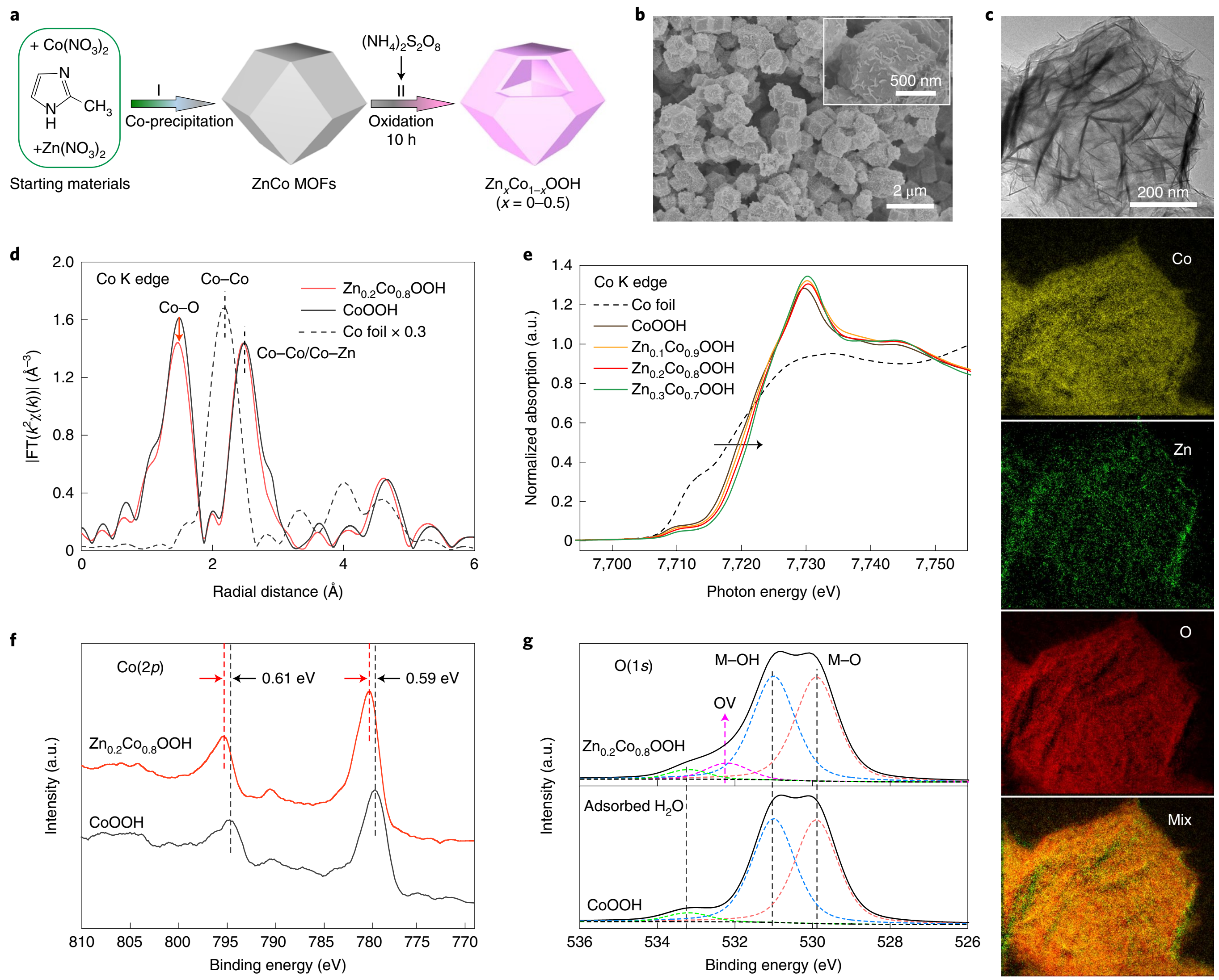

Fig. 3 | Design and structural characterization of zinc-substituted CoOOH. **a**, Schematic of the preparation process for zinc-substituted CoOOH. **b**,**c**, SEM image (**b**) and TEM image and STEM-EELS elemental mapping (**c**) of $Zn_{0.2}Co_{0.8}OOH$. The scale bar shown for the TEM image (top in **b**) also applies for the STEM-EELS maps (bottom four images in **b**). **d**,**e**, EXAFS $k^2\chi(k)$ Fourier transform (FT) spectra (**d**) and normalized cobalt K-edge XANES spectra (**e**) of $Zn_xCo_{1-x}OOH$ (where $x=0$, 0.1, 0.2 and 0.3) with cobalt foil as a reference. **f**,**g**, Co(2p) XPS spectra (**f**) and O(1s) XPS spectra (**g**) of $Zn_{0.2}Co_{0.8}OOH$ and CoOOH. OV, oxygen vacancy.

As the zinc amount increases, the adsorption edges defined by the half-height approach[43] are positively shifted towards higher energy than CoOOH, corresponding to the gradual increase in the valence state of cobalt (higher than a 3+ valence state). XPS spectra (Fig. 3f,g) also confirm the increased valence state of cobalt and the appearance of oxygen vacancies on the surface after incorporating zinc, which can be seen from the positive shift (about 0.60 eV) of binding energy for cobalt and the new peak at 532.3 eV for oxygen[44,45].

The iodometry[8] was used to quantitatively study the valence state of cobalt and the concentration of oxygen vacancies (the results are presented in Supplementary Table 4). As seen, the valence state of cobalt is increased from 2.98 to 3.60 as more Zn^{2+} ions (from $x=0$ to $x=0.5$) are used to substitute for octahedral Co^{3+}. That is, some high-valence Co^{4+} species have been detected in $Zn_xCo_{1-x}OOH$. An increase in the concentration of oxygen vacancies ($Zn_xCo_{1-x}O_{2-\delta}H$, where δ increases from 0 to 0.1) is observed as well. Both the increased valence state of cobalt and the appearance of oxygen vacancies from the bulk to the surface reveal the saturated charge states of cobalt after incorporating zinc[8–10]. As mentioned previously, the OH^-(aq.) tends to spontaneously fill the oxygen vacancy sites of $Zn_xCo_{1-x}O_{2-\delta}H$ under electrochemical OER conditions (Fig. 2b). On further electrochemical deprotonation, the oxygen ions around zinc would begin to be oxidized, producing oxygen holes in O_{NB} states.

Electrocatalytic OER measurement

Figure 4a shows the current- and resistance- (*iR*)-corrected polarization curves of $Zn_xCo_{1-x}OOH$ in 1 M KOH solution, together with CoOOH and IrO_2 for comparison (the experimental details are shown in Supplementary Fig. 15 and the Methods). To exclude geometric effects[46], the currents are normalized by Brunauer–Emmett–Teller (BET) surface areas (Supplementary Table 5). The overpotentials for reaching a specific current density of 0.1 mA cm^{-2}_{ox} are used for activity comparison. The value obtained for CoOOH is 385 mV, which is consistent with previous studies[35,40]. On incorporating zinc, the overpotentials are significantly decreased to 301 and 241 mV for $Zn_{0.1}Co_{0.9}OOH$ and $Zn_{0.2}Co_{0.8}OOH$, respectively. However, higher Zn/Co ratios (where $x=0.3$, 0.4 and 0.5) compared

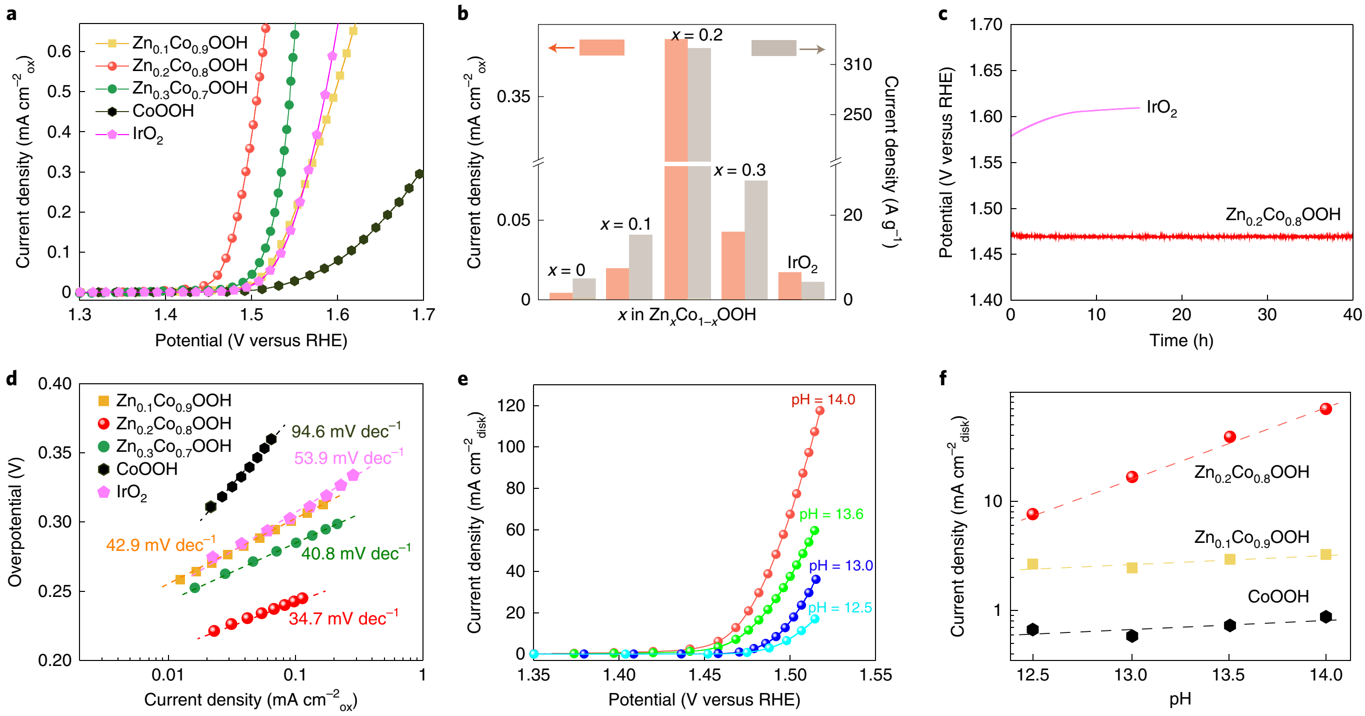

Fig. 4 | Electrocatalytic OER measurements. **a**, Polarization curves (current normalized by oxide BET surface area) of the as-synthesized $Zn_xCo_{1-x}OOH$, with IrO_2 as a comparison. **b**, Comparison of the normalized current densities based on BET surface area and mass at 1.5 V versus RHE. **c**, Galvanostatic stability of the OER at the geometric current density of 20 mA cm$^{-2}_{disk}$ over $Zn_{0.2}Co_{0.8}OOH$ loaded on carbon paper. **d**, Tafel plots. **e**, pH dependence of the OER activities of $Zn_{0.2}Co_{0.8}OOH$. **f**, Current densities of $Zn_{0.1}Co_{0.9}OOH$, $Zn_{0.2}Co_{0.8}OOH$ and CoOOH at 1.5 V versus RHE as a function of the pH value.

with $Zn_{0.2}Co_{0.8}OOH$ increase the overpotentials to 285, 297 and 351 mV, respectively (Fig. 4a and Supplementary Fig. 16a). Figure 4b further summarizes the specific current densities of the as-synthesized $Zn_xCo_{1-x}OOH$, CoOOH and IrO_2 at 1.50 V versus the reversible hydrogen electrode (RHE). As seen, $Zn_{0.2}Co_{0.8}OOH$ gives the highest intrinsic (mass) activity of 0.38 mA cm$^{-2}_{ox}$ (331.1 A g^{-1}), which is 38 (61) and 19 (75) times higher than CoOOH and IrO_2, respectively. Additionally, $Zn_{0.2}Co_{0.8}OOH$ shows an overpotential of 235 mV at the geometric current density of 10 mA cm$^{-2}_{disk}$, which is comparable and even lower than most of the transition metal-based catalysts previously reported (Supplementary Fig. 17 and Supplementary Table 6)[47–49]. For stability, $Zn_{0.2}Co_{0.8}OOH$ shows a negligible change of OER potential at 20 mA cm$^{-2}_{disk}$ after 40 h continuous testing (Fig. 4c). In contrast, IrO_2 at the same loading shows evidently decreased activity throughout the 10 h test, which might be due to the formation of highly oxidized iridates in alkaline environments[8]. In addition, the Faradaic efficiency of near-unity is measured for $Zn_{0.2}Co_{0.8}OOH$ (Supplementary Fig. 18), indicating that the measured current primarily originated from the water oxidation.

Tafel plots (Fig. 4d and Supplementary Fig. 16b) provide further information on the reaction mechanism[19,49]. $Zn_xCo_{1-x}OOH$ (where $x = 0.1$, 0.2, 0.3 and 0.4) shows decreased Tafel slopes of 42.9, 35.7, 40.8 and 45.7 mV dec^{-1}, respectively, compared with CoOOH (94.6 mV dec^{-1}), indicating a possible change in the PDS from the formation of *OOH to the deprotonation of *OH[49]. Previous calculations have suggested that the OER on both $Zn_{0.1}Co_{0.9}OOH$ and CoOOH proceeds via the AEM pathway, whereas, when incorporating more Zn^{2+} ($x \geq 0.2$), the emerged Zn–O2–Co–O2–Zn enables a switch of the OER mechanism to the LOM (Fig. 2b). The experimental validation of such a mechanism change is discussed in the section 'Chemical recognition of peroxo-like species'. In contrast, lower intrinsic activities of $Zn_{0.3}Co_{0.7}OOH$ and $Zn_{0.4}Co_{0.6}OOH$ compared with $Zn_{0.2}Co_{0.8}OOH$ would arise from their decreased number of Zn–O2–Co–O2–Zn structures. $Zn_{0.5}Co_{0.5}OOH$ shows a high Tafel slope of 82.1 mV dec^{-1}, approaching that of CoOOH (Supplementary Fig. 16b). As mentioned, the unfavourable energetics of oxygen vacancy refilling for $Zn_{0.5}Co_{0.5}OOH$ could lead to severe degradation (Fig. 2b). Therefore, both the high Tafel slope and poor intrinsic activity could be from the reconstructed phase (Supplementary Fig. 19), not reflecting the real case of $Zn_{0.5}Co_{0.5}OOH$. The XRD pattern and ICP measurement (Supplementary Fig. 20a and Table 2) confirm the reconstruction into spinel $ZnCo_2O_4$. Similar surface decompositions and reconstruction phenomena can be found for the reported electrocatalytic and battery materials, such as $Ba_xSr_{1-x}Co_yFe_{1-y}O_{3-\delta}$ and $Li_{1+x}Ni_yCo_zMn_{(1-x-y-z)}O_2$ due to the reactive oxygen states too close to the Fermi level[26,29,50–52]. Conversely, the values of x ($x = 0.1$, 0.2, 0.3 and 0.4) from ICP measurements (Supplementary Table 2), XRD and TEM characterization (Supplementary Fig. 20) in post-cycled $Zn_xCo_{1-x}OOH$ are almost identical to the initial ones.

The OER proceeding on oxides via the participation of lattice oxygen typically exhibits pH-dependent activity at the RHE scale[9]. Only the slowest step in the catalytic cycle is experimentally accessible; thus, the pH dependence can reflect the concerted or non-concerted proton–electron transfer step of the PDS[53]. The mismatch between the electron transfer kinetics and hydroxide affinity at the oxide/electrolyte interface contributes to the pH-dependent activity[54]. The conventional understanding of the AEM on oxides involves four concerted proton–electron transfer steps on metal-ion centres at their surface[9]. As evidenced, both OER activities of CoOOH and $Zn_{0.1}Co_{0.9}OOH$ exhibit negligible pH dependence (Supplementary Fig. 21). With an increase in the zinc amount, the electron transfer step should be accelerated, because the energy of O_{NB} states at E_F tends to fall below the O_2/H_2O redox couple (Fig. 1d,e), eliminating the barrier for electron transfer associated with the OER. Actually, the electrical conductivity measurements (Supplementary Fig. 22) confirm the enhanced

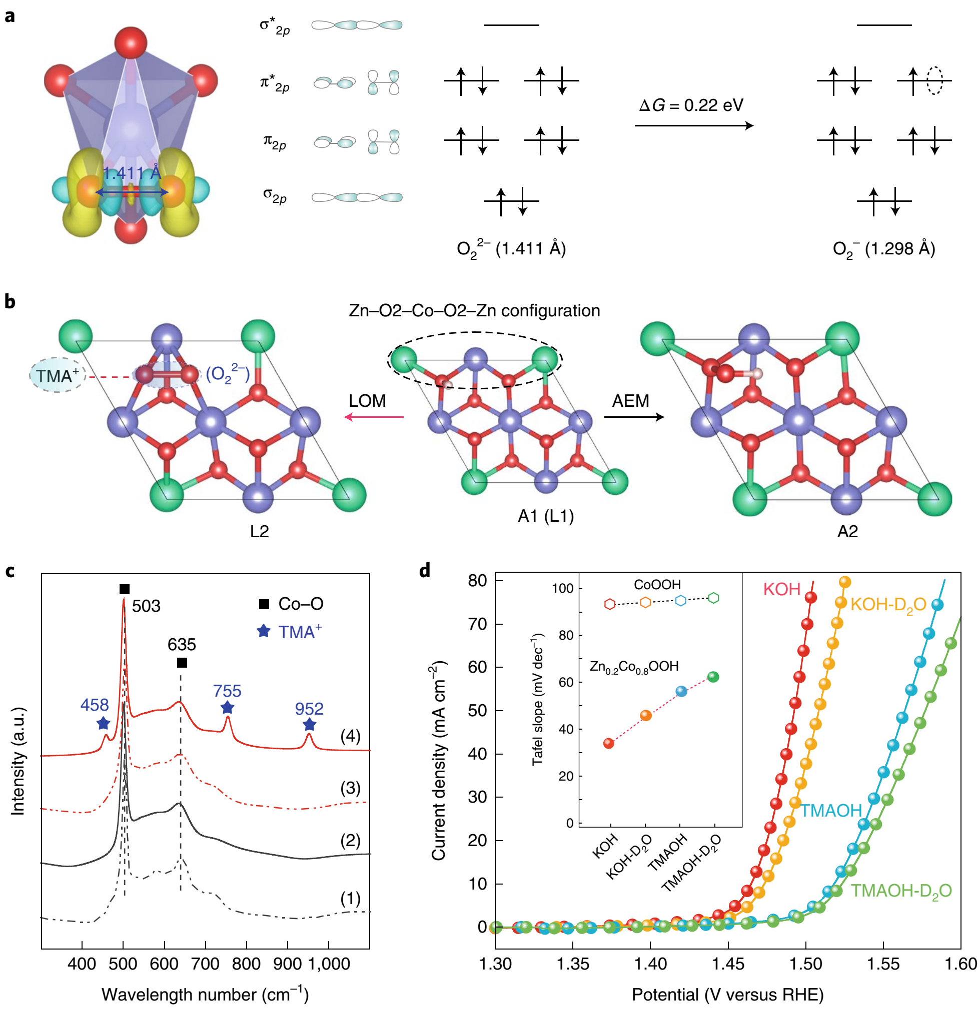

Fig. 5 | Chemical recognition of peroxo-like species from the LOM. a, Thermodynamic stabilities between O_2^{2-} and O_2^- species. Yellow and blue colours represent charge accumulation and depletion, respectively, with an iso-surface value of 0.015 eÅ^{-3}. **b**, Schematic of the chemical recognition of O_2^{2-} species using TMA$^+$ as a probe. **c**, Raman spectra of CoOOH (1 and 2) and $Zn_{0.2}Co_{0.8}OOH$ (3 and 4) electrodes. First, 1 and 3 were operated at the open-circuit potential, and 2 and 4 were operated at 1.45 V versus RHE, in 1 M TMAOH solution. Then, these electrodes were thoroughly washed by rinsing with high-purity water and acetone for ex situ Raman measurement. **d**, Polarization curves and derived Tafel slopes (inset) of $Zn_{0.2}Co_{0.8}OOH$ in 1 M KOH and TMAOH dissolved in H_2O or D_2O (99%), respectively.

conductivity of CoOOH with an increase in the zinc amount. As such, $Zn_{0.2}Co_{0.8}OOH$ shows strong pH dependence of around 68.1 decade pH^{-1} on the RHE scale (Fig. 4e,f), indicating that the non-concerted proton–electron transfer process for the OER can be triggered in a low concentration of hydroxyl ions. This similar phenomenon is also reported for $La_{0.5}Sr_{0.5}CoO_{3-\delta}$, $Pr_{0.5}Ba_{0.5}CoO_{3-\delta}$, $SrCoO_{3-\delta}$ and Ni–Fe–Cu metal/metal oxide[9,55]. We further propose one possible decoupled route (note that it is an extreme case for the transfer of severely limited hydroxyl ions compared with the electron transfer), which is displayed in Supplementary Fig. 23. The deprotonation ($HO–Co(O)–OH + OH^- \rightarrow HO–Co(O)–O + H_2O$) proceeds after the decoupled electron transfer during the release of oxygen ($HO–Co(O)–OO \rightarrow HO–Co(O)–\square + O_2 + e^-$, where the empty square represents the oxygen vacancy). The free energy change for the PDS of LOM increases evidently, from 0.27 eV for a concerted route to 0.77 eV for the given non-concerted route, due to the restriction of the hydroxyl exchange, consistent with the experimental results (Fig. 4e,f).

Chemical recognition of peroxo-like species

Recognition of peroxo-like (O_2^{2-}) and superoxo-like (O_2^-) negative species could provide indirect evidence for the proposed LOM pathway[29]. We first calculated the energetics to produce these species on $Zn_{0.2}Co_{0.8}OOH$. The free energy difference between these O_2^{2-} and O_2^- species is positive, with a value of 0.22 eV (Fig. 5a), indicating that O_2^{2-} is thermodynamically more stable than O_2^-. Therefore, there is an opportunity to directly probe the negative O_2^{2-} species during the OER catalytic process. The difference in the electronic configuration of these oxygenated species (Fig. 5a and Supplementary Fig. 24) is the unpaired electron in the π* orbital of the O_2^- ions[29]. As shown in the optimized adsorption structure, the O_2^{2-} species (1.411 Å) remains covalently bonded to the transition metal in which the π-symmetric orbitals of O_2^{2-} species could have net overlap with Co(t_{2g}) orbitals with the new structure rearrangement[29].

To track these negative O_2^{2-} species from the LOM[30,56,57], tetramethylammonium cation (TMA$^+$) as a chemical probe (Fig. 5b) is introduced to the solution because of its specific interaction with negative oxygenated species. As shown in Fig. 5c, two broad Raman peaks at 503 and 635 cm^{-1} were assigned to Co–O bonds for cobalt-based oxyhydroxides after the electrodes were pretreated at the open-circuit voltage state[44]. Three peaks appearing at 458, 755 and 952 cm^{-1}, which coincide with the characteristic peaks of TMA$^+$, are only observed on the $Zn_{0.2}Co_{0.8}OOH$ electrode pretreated with anodic polarization under 1.45 V versus RHE in the 1 M tetramethylammonium hydroxide (TMAOH) electrolyte[56]. This indicates that TMA^+ strongly binds to the $Zn_{0.2}Co_{0.8}OOH$ surface through the in situ generated negative oxygenated species during electrocatalytic water oxidation, and the oxidization of O_{NB} states due to the introduction of Zn^{2+} is responsible for inducing such species after the deprotonation. We further compare the OER activities of CoOOH and $Zn_{0.2}Co_{0.8}OOH$ electrodes in 1 M KOH and TMAOH solutions. As shown in Fig. 5d, $Zn_{0.2}Co_{0.8}OOH$ exhibits significantly reduced OER activity and its Tafel slope is increased from 34.7 to 58.0 mV dec^{-1} (inset in Fig. 5d) because of the inhibition of the LOM with strong binding of TMA^+, while CoOOH shows very minimal change. To further elucidate the mechanism on $Zn_{0.2}Co_{0.8}OOH$, the OER measurements were also performed in D_2O solutions (Fig. 5d)[56]. The use of D_2O significantly decreases the OER activity of $Zn_{0.2}Co_{0.8}OOH$ in KOH solution and TMAOH with increased Tafel slopes, validating the proposed PDS of deprotonation in both LOM and AEM pathways from free-energy calculations (Fig. 2b). In contrast, CoOOH shows very minimal change when D_2O is used, indicating that the PDS is not the deprotonation step, consistent with the free-energy calculation (the calculated PDS is the formation of *OOH, as shown in Fig. 2b).

Conclusions

We have employed zinc-substituted CoOOH with different amounts of Zn^{2+} as model catalysts for the OER and suggest that the OER mechanism can be switched from the AEM to the LOM only if two neighbouring oxidized oxygen atoms can hybridize their oxygen holes without sacrificing metal–oxygen hybridization significantly. In particular, the carefully designed catalyst $Zn_{0.2}Co_{0.8}OOH$ with the Zn–O2–Co–O2–Zn configuration manifested the optimized activity. Raman spectra with chemical probe analysis further identified the negative peroxo-like species from the LOM. Additionally, the specific Zn–O2–Co–O2–Zn configuration provides a balance between direct O–O coupling and oxygen vacancy refilling, maintaining the stability of the catalyst. This work provides a guideline for the development of efficient and stable catalysts towards water oxidation and other heterogeneous catalysis involving lattice oxygen.

Methods

Materials. $Co(NO_3)_2{\cdot}6H_2O$, $Zn(NO_3)_2{\cdot}6H_2O$ and $(NH_4)_2S_2O_8$ were obtained from J&K Chemical. Methanol, absolute ethanol and isopropanol were obtained from the Chemicals Testing and Calibration Laboratory. Nafion solution (~5 wt.%), TMAOH (~25 wt.% in H_2O), D_2O (≥99.96 at.% D) and 2-methylimidazole were obtained from Sigma–Aldrich. All of the chemicals were reagent grade and used as received. High-purity water (18.25 MΩ·cm) supplied by a Milli-Q Gradient A10 system was used in all of the experiments.

Synthesis of zinc-substituted CoOOH. First, bimetallic MOFs were prepared using a previously reported modified co-precipitation method[39]. In detail, $Co(NO_3)_2{\cdot}6H_2O$ and $Zn(NO_3)_2{\cdot}6H_2O$ with the desired zinc amount ($x = 0.1$, 0.2, 0.3, 0.4 or 0.5) were dissolved in 30 ml of methanol to form a clear solution, which was subsequently poured into 20 ml of methanol containing 2-methylimidazole (1.97 g). After thorough mixing, the solution was incubated at room temperature for 24 h. The total molar amount of (Zn + Co) was fixed to be 3 mmol. The as-obtained precipitates were centrifuged and washed with ethanol several times, and finally dried under vacuum for 12 h, resulting in so-called ZnCo MOFs. Then, these MOFs as both precursor and self-template were topologically converted into cobalt-based oxyhydroxides (denoted as $Zn_xCo_{1-x}OOH$) by hydrothermal oxidation[58]. In detail, 80 mg ZnCo MOFs were redispersed into 40 ml H_2O, followed by the addition of 0.15 g $(NH_4)_2S_2O_8$ with constant agitation for 30 min. Thereafter, the mixture was transferred into a Teflon-lined stainless steel autoclave and heated at 100 °C for 10 h. The formed $Zn_xCo_{1-x}OOH$ was centrifuged and washed with ethanol several times, then the products were dried under vacuum for 12 h before use. As a comparison, CoOOH and $ZnCo_2O_4$ were also synthesized. In detail, for CoOOH, ZIF-67 was used as a precursor following a procedure similar to zinc-substituted CoOOH. For $ZnCo_2O_4$, the powders of MOFs with a Zn:Co ratio of 1:2 were placed in a tube furnace, then heated to 400 °C for 30 min with a ramp of 5 °C min^{-1} under N_2 gas flow. After that, the N_2 gas was switched off, and the furnace was inflated with air and kept at this temperature for another 30 min. Finally, the product was taken out after its colour changed from pink to black.

Considering that the hydrothermal treatment step may cause certain limitations on the scalability of the process, we managed to replace it with a refluxing step. Taking $Zn_{0.2}Co_{0.8}OOH$ as an example, 3.0 g ZnCo MOFs ($x = 0.2$) were redispersed into 250 ml H_2O, followed by the addition of 1.54 g $(NH_4)_2S_2O_8$ with constant agitation for 60 min. Thereafter, the mixtures were transferred into a round-bottom flask under stirring and heated at 100 °C with refluxing until the purple colour disappeared entirely. The formed $Zn_xCo_{1-x}OOH$ was centrifuged and washed with ethanol several times, then the products were dried under vacuum for 12 h before use. As such, we were able to obtain a yield of 95% and a quantity at the gram level (Supplementary Fig. 25).

Composition and structure characterization. XRD was recorded with a Bruker D8 FOCUS operating at 40 kV and 40 mA equipped with nickel-filtered Cu Kα radiation (λ = 1.541 Å). Field emission SEM images were obtained using a Hitachi S-4800 SEM. Transmission electron microscopy (TEM) images and EELS element mapping were obtained using a JEM-2100F transmission electron microscope at 200 kV. Element composition was analysed using a Vista-MPX EL02115765 ICP atomic emission spectrometer. The BET surface area was determined using N_2 sorption isotherm measurements at −196 °C on Micrometrics TriStar 3000 equipment. XPS data were obtained on a PHI 1600 instrument equipped with Al Kα radiation. Raman spectra were acquired on a Thermo Nicolet 6700 FT-Raman Spectrophotometer with an exciting wavelength of 325 nm. Cobalt L-edge X-ray absorption spectra were collected at the XAFS beamline at the Singapore Synchrotron Light Source using the transmission mode. Acquired EXAFS data were processed according to standard procedures using the ATHENA module implemented in the IFEFFIT software packages[59]. The k^2-weighted Fourier transforms for all of the EXAFS data were conducted in the k-range 2–12 $Å^{-1}$ using a Hanning-shaped window. The S_0^2, used in the fitting for cobalt, was based on CoOOH and fixed to be 0.78 for the other samples. The k- and *R*-ranges for the fitting of all of the EXAFS data were set as 2–12 $Å^{-1}$ and 1.0–3.5 Å, respectively.

The contents of oxygen vacancies were determined by iodimetry based on oxidation–reduction titrations[8]. The process was as follows. An accurately weighed amount (m) of the sample in a 250 ml conical flask was dissolved in 10 ml of an aqueous solution containing 0.7 g KI with N_2 as the shielding gas. After adding 7 ml of a HCl solution (6 M), 50 ml water was added to dilute the solution. A starch indicator and the calibration concentration (C) of an $Na_2S_2O_3$ solution were used to directly titrate the mixture described above. The consumed volume of $Na_2S_2O_3$ (V) was recorded. The oxygen vacancies (δ) were calculated according to equations (1) and (2):

$$\begin{aligned}&Zn_xCo_{1-x}O_{2-\delta}H + (3-2\delta)H^+ + (1-2\delta)I^- \rightarrow xZn^{2+}\\&+(1-x)Co^{3+} + (2-\delta)H_2O + (0.5-\delta)I_2\end{aligned} \tag{1}$$

$$2S_2O_3^{2-} + I_2 \rightarrow S_4O_6^{2-} + 2I^- \tag{2}$$

For the electrical conductivity measurement, the samples were pressed into thin slices under 2 MPa, then the resistances (R) were measured using a Keithley model 2000 multimeter instrument. The electrical conductivities (σ) of the samples were calculated through $R = \rho L/S$ and $\sigma = 1/\rho$, where ρ, L and S represent the electrical resistivity, thickness and area of the pressed sample, respectively.

Electrochemical measurements. All of the electrochemical measurements were conducted using an Autolab PGSTAT302 potentiostat and a Pine rotating disk electrode apparatus in a typical three-electrode setup with 1 M KOH solution as the electrolyte, a graphite rod as the counter electrode and Ag/AgCl with saturated KCl filling solution as the reference electrode. The as-measured potentials (versus Ag/AgCl) were calibrated with respect to the RHE. A glassy carbon electrode with a diameter of 5 mm covered by a thin catalyst film was used as the working electrode. Typically, 4 mg catalyst and 0.8 mg acetylene black were suspended in 2 ml isopropanol-water solution with a volume ratio of 3:1 with 100 µl Nafion solution to form a homogeneous ink assisted by ultrasound for 3 h. Then, 20 µl of the ink was spread onto the surface of the glassy carbon electrode (mass loading: 0.204 mg cm^{-2}) by a micropipette and dried under room temperature. For linear sweep voltammetry measurements, the scan rate was set to 2 mV s^{-1} at a rotational speed of 1,600 r.p.m. to reduce the influence of capacitive current and gas bubbles. The potentials were corrected to compensate for the effect of solution resistance and calculated using the following equation: $E_{iR\ \mathrm{corrected}} = E - iR_s$, where R_s is the uncompensated ohmic solution resistance (5.4 Ω) measured via high-frequency a.c. impedance in 1 M KOH. The polarization curves were plotted as the overpotential (η) versus the log current ($\log[J]$) to obtain the Tafel plots. The Tafel slope (b) was obtained by fitting the linear portion of the Tafel plots to the Tafel equation ($\eta = b\log[J] + a$).

The Faradic efficiency is defined as the ratio of the amount of experimentally determined O_2 to that of the theoretically expected O_2 from the reaction. The amount of evolved O_2 was monitored using a gas chromatograph. As for the theoretical value, we assumed 100% current efficiency during the reaction, which meant that only the OER process was occurring at the working electrode. The theoretically expected amount of O_2 was then calculated by applying the Faraday law, which states that the passage of 96,485.4C causes 1 equivalent of reaction. The Faradic efficiency (FE) was also obtained using the rotating ring-disk electrode technique according to equation (3):

$$FE = i_{\mathrm{disk}} \; / \; (Ce \times i_{\mathrm{ring}}) \qquad (3)$$

where i_{disk} is the given current on the disk electrode, i_{ring} is the collection current on the platinum ring electrode at a constant potential of 0.4 V versus RHE, and Ce is the oxygen collection coefficient, which was determined to be ~0.2.

Computational models and methods. The CoO_2(001)-terminated surface was chosen as a computation model with Co^{4+} located on the octahedral site[25,30]. Zinc was introduced afterwards by replacing partial cobalt atoms (denoted as $Zn_xCo_{1-x}O_2$, where $x=0.1$, 0.2 or 0.5) to further regulate the electronic states. $Zn_{0.2}Co_{0.8}O_2$ and $Zn_{0.5}Co_{0.5}O_2$ were established based on the 2 × 2 CoO_2 supercell, whereas $Zn_{0.1}Co_{0.9}O_2$ was established based on the 3 × 3 CoO_2 supercell. The constructed supercell was isolated with a 15 Å vacuum space in the z direction. All POSCAR files of models are shown in Supplementary Data 1.

All density functional theory (DFT) calculations were performed with the Vienna Ab initio Simulation Package using spin-polarized DFT with the Hubbard model (DFT+U)[60,61]. The projector augmented wave pseudopotential with the revised Perdew–Burke–Ernzerhof exchange-correlation functional was used[62,63]. For a better description of the Co(3d) and Zn(3d) electrons[64,65], the effective U values of 8.5 and 4.0 eV were applied, respectively. A kinetic energy cut-off of 500 eV was used. The Brillouin zones of all systems were sampled with Gamma-point-centred Monkhorst–Pack grids. The 5 × 5 × 1 and 3 × 3 × 1 Monkhorst–Pack k-point setups were used for 2 × 2 and 3 × 3 supercell structure optimization, respectively. The more refined separation 7 × 7 × 1 and 5 × 5 × 1 Monkhorst–Pack k-point meshes were used for the electronic structure calculations of 2 × 2 and 3 × 3 supercells. The force and energy convergence criteria were set to 0.02 eV $Å^{-1}$ and 10^{-5} eV, respectively. The DFT-D3 method with Becke–Jonson damping was adopted to consider van der Waals correction[66,67]. Transition states were searched using the climbing image nudged elastic band method, with four images along each path[68,69], and verified with only one imaginary frequency.

Data availability

The data that support the plots within this paper and other finding of this study are available from the corresponding authors upon reasonable request.

Received: 28 August 2018; Accepted: 15 February 2019;

References

1. Hwang, J. et al. Perovskites in catalysis and electrocatalysis. *Science* **358**, 751–756 (2017).
2. Seh, Z. W. et al. Combining theory and experiment in electrocatalysis: insights into materials design. *Science* **355**, eaad4998 (2017).
3. Xia, B. Y. et al. A metal–organic framework-derived bifunctional oxygen electrocatalyst. *Nat. Energy* **1**, 15006 (2016).
4. Vojvodic, A. & Norskov, J. K. Optimizing perovskites for the water-splitting reaction. *Science* **334**, 1355–1356 (2011).
5. Man, I. C. et al. Universality in oxygen evolution electrocatalysis on oxide surfaces. *ChemCatChem* **3**, 1159–1165 (2011).
6. Huang, Z.-F. et al. Design of efficient bifunctional oxygen reduction/evolution electrocatalyst: recent advances and perspectives. *Adv. Energy Mater.* **7**, 1700544 (2017).
7. Montoya, J. H. et al. Materials for solar fuels and chemicals. *Nat. Mater.* **16**, 70–81 (2016).
8. Mefford, J. T. et al. Water electrolysis on $La_{1-x}Sr_xCoO_3$ perovskite electrocatalysts. *Nat. Commun.* **7**, 11053 (2016).
9. Grimaud, A. et al. Activating lattice oxygen redox reactions in metal oxides to catalyse oxygen evolution. *Nat. Chem.* **9**, 457–465 (2017).
10. Rong, X., Parolin, J. & Kolpak, A. M. A fundamental relationship between reaction mechanism and stability in metal oxide catalysts for oxygen evolution. *ACS Catal.* **6**, 1153–1158 (2016).
11. Yagi, S. et al. Covalency-reinforced oxygen evolution reaction catalyst. *Nat. Commun.* **6**, 8249 (2015).
12. Forslund, R. P. et al. Exceptional electrocatalytic oxygen evolution via tunable charge transfer interactions in $La_{0.5}Sr_{1.5}Ni_{1-x}Fe_xO_{4\pm\delta}$ Ruddlesden–Popper oxides. *Nat. Commun.* **9**, 3150 (2018).
13. Cheng, X. et al. Oxygen evolution reaction on $La_{1-x}Sr_xCoO_3$ perovskites: a combined experimental and theoretical study of their structural, electronic, and electrochemical properties. *Chem. Mater.* **27**, 7662–7672 (2015).
14. Yoo, J. S., Rong, X., Liu, Y. S. & Kolpak, A. M. Role of lattice oxygen participation in understanding trends in the oxygen evolution reaction on perovskites. *ACS Catal.* **8**, 4628–4636 (2018).
15. Fabbri, E. & Schmidt, T. J. Oxygen evolution reaction—the enigma in water electrolysis. *ACS Catal.* **8**, 9765–9774 (2018).
16. Nie, L. et al. Activation of surface lattice oxygen in single-atom Pt/CeO_2 for low-temperature CO oxidation. *Science* **358**, 1419–1423 (2017).
17. McCalla, E. et al. Visualization of O–O peroxo-like dimers in high-capacity layered oxides for Li-ion batteries. *Science* **350**, 1516–1521 (2015).
18. McCrory, C. C., Jung, S., Peters, J. C. & Jaramillo, T. F. Benchmarking heterogeneous electrocatalysts for the oxygen evolution reaction. *J. Am. Chem. Soc.* **135**, 16977–16987 (2013).
19. Song, F. et al. Transition metal oxides as electrocatalysts for the oxygen evolution reaction in alkaline solutions: an application-inspired renaissance. *J. Am. Chem. Soc.* **140**, 7748–7759 (2018).
20. Jiao, Y., Zheng, Y., Jaroniec, M. & Qiao, S. Z. Design of electrocatalysts for oxygen- and hydrogen-involving energy conversion reactions. *Chem. Soc. Rev.* **44**, 2060–2086 (2015).
21. Dionigi, F. & Strasser, P. NiFe-based (oxy)hydroxide catalysts for oxygen evolution reaction in non-acidic electrolytes. *Adv. Energy Mater.* **6**, 1600621 (2016).
22. Fabbri, E. et al. Dynamic surface self-reconstruction is the key of highly active perovskite nano-electrocatalysts for water splitting. *Nat. Mater.* **16**, 925–931 (2017).
23. Han, B. et al. Nanoscale structural oscillations in perovskite oxides induced by oxygen evolution. *Nat. Mater.* **16**, 121–126 (2017).
24. Xu, X., Song, F. & Hu, X. A nickel iron diselenide-derived efficient oxygen-evolution catalyst. *Nat. Commun.* **7**, 12324 (2016).
25. Favaro, M. et al. Understanding the oxygen evolution reaction mechanism on CoO_x using operando ambient-pressure X-ray photoelectron spectroscopy. *J. Am. Chem. Soc.* **139**, 8960–8970 (2017).
26. Grimaud, A., Hong, W. T., Shao-Horn, Y. & Tarascon, J. M. Anionic redox processes for electrochemical devices. *Nat. Mater.* **15**, 121–126 (2016).
27. Zhou, Y. et al. Superexchange effects on oxygen reduction activity of edge-sharing $[Co_xMn_{1-x}O_6]$ octahedra in spinel oxide. *Adv. Mater.* **30**, 1705407 (2018).
28. Seo, D. H. et al. The structural and chemical origin of the oxygen redox activity in layered and cation-disordered Li-excess cathode materials. *Nat. Chem.* **8**, 692–697 (2016).
29. Assat, G. & Tarascon, J. M. Fundamental understanding and practical challenges of anionic redox activity in Li-ion batteries. *Nat. Energy* **3**, 373–386 (2018).
30. Zhang, M., de Respinis, M. & Frei, H. Time-resolved observations of water oxidation intermediates on a cobalt oxide nanoparticle catalyst. *Nat. Chem.* **6**, 362–367 (2014).
31. Maitra, U. et al. Oxygen redox chemistry without excess alkali-metal ions in $Na_{2/3}[Mg_{0.28}Mn_{0.72}]O_2$. *Nat. Chem.* **10**, 288–295 (2018).
32. Shin, H., Xiao, H. & Goddard, W. A. In silico discovery of new dopants for Fe-doped Ni oxyhydroxide ($Ni_{1-x}Fe_xOOH$) catalysts for oxygen evolution reaction. *J. Am. Chem. Soc.* **140**, 6745–6748 (2018).
33. Grimaud, A. et al. Activation of surface oxygen sites on an iridium-based model catalyst for the oxygen evolution reaction. *Nat. Energy* **2**, 16189 (2016).
34. Yoo, J. S., Liu, Y., Rong, X. & Kolpak, A. M. Electronic origin and kinetic feasibility of the lattice oxygen participation during the oxygen evolution reaction on perovskites.*J. Phys. Chem. Lett.* **9**, 1473–1479 (2018).
35. Zhang, B. et al. Homogeneously dispersed multimetal oxygen-evolving catalysts. *Science* **352**, 333–337 (2016).
36. Grimaud, A. et al. Double perovskites as a family of highly active catalysts for oxygen evolution in alkaline solution. *Nat. Commun.* **4**, 2439 (2013).
37. Xie, Y., Saubanère, M. & Doublet, M. L. Requirements for reversible extra-capacity in Li-rich layered oxides for Li-ion batteries. *Energy Environ. Sci.* **10**, 266–274 (2017).
38. Xiao, H., Shin, H. & Goddard, W. A. Synergy between Fe and Ni in the optimal performance of (Ni,Fe)OOH catalysts for the oxygen evolution reaction. *Proc. Natl Acad. Sci. USA* **115**, 5872–5877 (2018).
39. Huang, Z.-F. et al. Hollow cobalt-based bimetallic sulfide polyhedra for efficient all-pH-value electrochemical and photocatalytic hydrogen evolution. *J. Am. Chem. Soc.* **138**, 1359–1365 (2016).
40. Ye, S. H., Shi, Z. X., Feng, J. X., Tong, Y. X. & Li, G. R. Activating CoOOH porous nanosheet arrays by partial iron substitution for efficient oxygen evolution reaction. *Angew. Chem. Int. Ed.* **57**, 2672–2676 (2018).
41. Huang, J. et al. Oxyhydroxide nanosheets with highly efficient electron-hole pair separation for hydrogen evolution. *Angew. Chem. Int. Ed.* **55**, 2137–2141 (2016).
42. Wang, J. et al. Heterogeneous electrocatalyst with molecular cobalt ions serving as the center of active sites. *J. Am. Chem. Soc.* **139**, 1878–1884 (2017).
43. Dau, H., Liebisch, P. & Haumann, M. X-ray absorption spectroscopy to analyze nuclear geometry and electronic structure of biological metal centers—potential and questions examined with special focus on the tetra-nuclear manganese complex of oxygenic photosynthesis. *Anal. Bioanal. Chem.* **376**, 562–583 (2003).
44. Yang, J., Liu, H. W., Martens, W. N. & Frost, R. L. Synthesis and characterization of cobalt hydroxide, cobalt oxyhydroxide, and cobalt oxide nanodiscs. *J. Phys. Chem. C* **114**, 111–119 (2010).

45. Sun, Y., Gao, S., Lei, F. & Xie, Y. Atomically-thin two-dimensional sheets for understanding active sites in catalysis. *Chem. Soc. Rev.* **44**, 623–636 (2015).
46. Sun, S., Li, H. & Xu, Z. J. Impact of surface area in evaluation of catalyst activity. *Joule* **2**, 1024–1027 (2018).
47. Han, L., Dong, S. & Wang, E. Transition-metal (Co, Ni, and Fe)-based electrocatalysts for the water oxidation reaction. *Adv. Mater.* **28**, 9266–9291 (2016).
48. Lee, Y., Suntivich, J., May, K. J., Perry, E. E. & Shao-Horn, Y. Synthesis and activities of rutile IrO_2 and RuO_2 nanoparticles for oxygen evolution in acid and alkaline solutions. *J. Phys. Chem. Lett.* **3**, 399–404 (2012).
49. Suen, N. T. et al. Electrocatalysis for the oxygen evolution reaction: recent development and future perspectives. *Chem. Soc. Rev.* **46**, 337–365 (2017).
50. Sathiya, M. et al. Reversible anionic redox chemistry in high-capacity layered-oxide electrodes. *Nat. Mater.* **12**, 827–835 (2013).
51. Gent, W. E. et al. Coupling between oxygen redox and cation migration explains unusual electrochemistry in lithium-rich layered oxides. *Nat. Commun.* **8**, 2091 (2017).
52. Seitz, L. C. et al. A highly active and stable IrO_x/$SrIrO_3$ catalyst for the oxygen evolution reaction. *Science* **353**, 1011–1014 (2016).
53. Giordano, L. et al. pH dependence of OER activity of oxides: current and future perspectives. *Catal. Today* **262**, 2–10 (2016).
54. Liu, T. et al. Accelerating proton-coupled electron transfer of metal hydrides in catalyst model reactions. *Nat. Chem.* **10**, 881–887 (2018).
55. Zhang, P. et al. Dendritic core-shell nickel-iron-copper metal/metal oxide electrode for efficient electrocatalytic water oxidation. *Nat. Commun.* **9**, 381 (2018).
56. Yang, C., Fontaine, O., Tarascon, J. M. & Grimaud, A. Chemical recognition of active oxygen species on the surface of oxygen evolution reaction electrocatalysts. *Angew. Chem. Int. Ed.* **56**, 8652–8656 (2017).
57. Trzesniewski, B. J. et al. In situ observation of active oxygen species in Fe-containing Ni-based oxygen evolution catalysts: the effect of pH on electrochemical activity. *J. Am. Chem. Soc.* **137**, 15112–15121 (2015).
58. Chen, C. H. et al. Controlled synthesis of self-assembled metal oxide hollow spheres via tuning redox potentials: versatile nanostructured cobalt oxides. *Adv. Mater.* **20**, 1205–1209 (2008).
59. Newville, M. IFEFFIT: interactive XAFS analysis and FEFF fitting. *J. Synchrotron Radiat.* **8**, 322–324 (2001).
60. Anisimov, V. I., Aryasetiawan, F. & Lichtenstein, A. First-principles calculations of the electronic structure and spectra of strongly correlated systems: the LDA + U method. *J. Phys. Condens. Matter* **9**, 767–808 (1997).
61. Anisimov, V. I., Zaanen, J. & Andersen, O. K. Band theory and Mott insulators: Hubbard U instead of Stoner I. *Phys. Rev. B* **44**, 943 (1991).
62. Blöchl, P. E. Projector augmented-wave method. *Phys. Rev. B* **50**, 17953–17979 (1994).
63. Hammer, B., Hansen, L. B. & Nørskov, J. K. Improved adsorption energetics within density-functional theory using revised Perdew–Burke–Ernzerhof functionals. *Phys. Rev. B* **59**, 7413 (1999).
64. Liao, P., Keith, J. A. & Carter, E. A. Water oxidation on pure and doped hematite (0001) surfaces: prediction of Co and Ni as effective dopants for electrocatalysis. *J. Am. Chem. Soc.* **134**, 13296–13309 (2012).
65. Zhou, G. et al. First-principle study on bonding mechanism of ZnO by LDA + U method. *Phys. Lett. A* **368**, 112–116 (2007).
66. Grimme, S., Ehrlich, S. & Goerigk, L. Effect of the damping function in dispersion corrected density functional theory. *J. Comput. Chem.* **32**, 1456–1465 (2011).
67. Grimme, S., Antony, J., Ehrlich, S. & Krieg, H. A consistent and accurate ab initio parametrization of density functional dispersion correction (DFT-D) for the 94 elements H–Pu. *J. Chem. Phys.* **132**, 154104 (2010).
68. Henkelman, G. & Jónsson, H. Improved tangent estimate in the nudged elastic band method for finding minimum energy paths and saddle points. *J. Chem. Phys.* **113**, 9978–9985 (2000).
69. Henkelman, G., Uberuaga, B. P. & Jónsson, H. A climbing image nudged elastic band method for finding saddle points and minimum energy paths. *J. Chem. Phys.* **113**, 9901–9904 (2000).

Acknowledgements

The authors appreciate the support from the National Research Foundation, Prime Minister's Office, Singapore, under its Campus for Research Excellence and Technological Enterprise (CREATE) programme. We also acknowledge financial support from the academic research fund AcRF Tier 2 (M4020246, ARC10/15), Ministry of Education, Singapore.

Author contributions

X.W., Z.J.X. and Z.-F.H. designed the studies and wrote the paper. Z.-F.H. synthesized the catalysts and performed the catalytic tests. Z.-F.H. and J.S. performed the density functional theory calculations. Z.-F.H., S.D., C.W. and J.M.V.N. conducted the SEM, STEM-EELS and XPS measurements. Y.D. and S.X. conducted the XAFS measurements. All authors discussed the results and commented on the manuscript.

Competing interests

The authors declare no competing interests.

Additional information

Supplementary information is available for this paper at https://doi.org/10.1038/s41560-019-0355-9.

Reprints and permissions information is available at www.nature.com/reprints.

Correspondence and requests for materials should be addressed to Z.J.X. or X.W.